Radiation Tolerance of Low-Noise Photoreceivers for the LISA Space Mission

P. Colcombet, N. Dinu-Jaeger, C. Inguimbert, T. Nuns, S. Bruhier, N. Christensen, P. Hofverberg, N. van Bakel, M. van Beuzekom, T. Mistry, G. Visser, D. Pascucci, K. Izumi, K. Komori, G. Heinzel, G. Fernández Barranco, J. J. M. in t Zand, P. Laubert, and M. Frericks

***Abstract*— This study investigates the effects of space environmental radiation on the performance of $In_{0.53}Ga_{0.47}As$ quadrant photodiodes (QPDs) and assesses their suitability for the laser interferometer space antenna (LISA) mission. QPDs of 1.0-, 1.5-, and 2.0-mm diameter were irradiated with 20- and 60-MeV protons, 0.5- and 1-MeV electrons, and Co^{60} gamma rays. An exposure corresponding to a displacement damage equivalent fluence (DDEF) of $1.0 \times 10 + 12 p/cm^2$ for 20- and 60-MeV protons and a total ionizing dose (TID) of 237 krad were applied, exceeding the radiation requirements for the LISA mission by a factor of approximately 5. Experiments were conducted to measure changes in QPD dark current, capacitance, and responsivity. The QPDs were integrated with a low-noise dc-coupled transimpedance amplifier (TIA) to form the quadrant photoreceiver (QPR). QPR noise and performance in an interferometric system like LISA were also performed. Although radiation impacted their dark current and responsivity, almost all QPDs met LISA's validation criteria and did not demonstrate any critical failure. These findings suggest that the tested QPDs are promising candidates for LISA and other space-based missions.**

***Index Terms*— InGaAs quadrant photodiodes (QPDs), ionizing dose, laser interferometer space antenna (LISA), nonionizing displacement dose, space environment.**

Manuscript received 25 April 2024; revised 8 May 2024; accepted 9 May 2024. Date of publication 14 May 2024; date of current version 16 August 2024. *(Corresponding author: P. Colcombet.)*

P. Colcombet is with the Observatoire de la Côte d'Azur, CNRS, ARTEMIS, Université Côte d'Azur, 06304 Nice, France, and also with DPHY, ONERA, The French Aerospace Laboratory, 31055 Toulouse, France (e-mail: paul.colcombet@oca.eu).

N. Dinu-Jaeger, S. Bruhier, and N. Christensen are with the Observatoire de la Côte d'Azur, CNRS, ARTEMIS, Université Côte d'Azur, 06304 Nice, France (e-mail: nicoleta.dinu-jaeger@oca.eu; sara.bruhier@gmail.com; nelson.christensen@oca.eu).

C. Inguimbert and T. Nuns are with DPHY, ONERA, The French Aerospace Laboratory, 31055 Toulouse, France (e-mail: christophe.inguimbert@onera.fr; thierry.nuns@onera.fr).

P. Hofverberg is with the Institut Méditerranéen De Protonthérapie, Center Antoine Lacassagne, 06200 Nice, France (e-mail: petter.hofverberg@gmail.com).

N. van Bakel, M. van Beuzekom, T. Mistry, G. Visser, and D. Pascucci are with the Nikhef Dutch National Institute for Subatomic Physics, 1098 XG Amsterdam, The Netherlands (e-mail: nielsvb@nikhef.nl; martinb@nikhef.nl; t.mistry@nikhef.nl; g.visser@nikhef.nl; d.pascucci@nikhef.nl).

K. Izumi and K. Komori are with Japan Aerospace Exploration Agency (JAXA), Tokyo 182-8522, Japan (e-mail: kiwamu@astro.isas.jaxa.jp; komori@jaxa.jp).

G. Heinzel and G. Fernández Barranco are with the Max Planck Institute for Gravitational Physics [Albert Einstein Institute(AEI)], 30167 Hannover, Germany (e-mail: gerhard.heinzel@aei.mpg.de; German.Fernandez.Barranco@aei.mpg.de).

J. J. M. in t Zand, P. Laubert, and M. Frericks are with the SRON Netherlands Institute for Space Research, 2333 CA Leiden, The Netherlands (e-mail: J.J.M.in.t.Zand@sron.nl; P.P.Laubert@sron.nl; M.Frericks@sron.nl).

Color versions of one or more figures in this article are available at https://doi.org/10.1109/TNS.2024.3401047.

Digital Object Identifier 10.1109/TNS.2024.3401047

I. Introduction

PLANNED for 2035 and led by the European Space Agency (ESA), laser interferometer space antenna (LISA) will be the first space-based gravitational-wave (GW) detector, operating in the frequency range of 10^{-4}–1 Hz. This low-frequency band, inaccessible to ground-based detectors, has the potential to open new frontiers in the study of the universe [1], [2], [3], [4].

LISA will consist of three spacecraft, arranged in an equilateral triangle with 2.5 million km arms, orbiting in the Earth-like heliocentric orbit at one astronomical unit from the Sun, and located at an angle of 20° behind the Earth. The detection of GWs is achieved by measuring the distance variations between free-fall test masses located in separate spacecraft, using high-precision laser interferometers operating at a wavelength of 1064 nm [5]. The interferometric signal detection in LISA is achieved with quadrant photoreceivers (QPRs), key for identifying interference between optical signals of disparate powers ∼700 pW and 1 mW. A QPR is composed of a quadrant photodiode (QPD) connected to a low-noise dc-coupled transimpedance amplifier (TIA) or front end electronics (FEE) assembled in a mechanical housing.

Throughout its mission, LISA will encounter diverse radiation types, which may affect the electrical properties of its QPD. This study focuses on the tolerance of QPD performance in terms of dark current, capacitance, and responsivity under proton, electron, and gamma-ray irradiation at LISA fluences and beyond. The study also examines the QPR noise, and optical performance related to the amplitude and the phase of the ac signals in an optical system, reproducing the LISA interferometers. This work will contribute to a comprehensive understanding of the impact of radiation on the QPD's electro-optical characteristics and the overall interferometric system performance.

II. Irradiation and Test Description

A. Tested QPD and QPR

The QPDs are custom $In_{0.53}Ga_{0.47}As$ (now referred to as InGaAs) devices developed for the LISA mission by

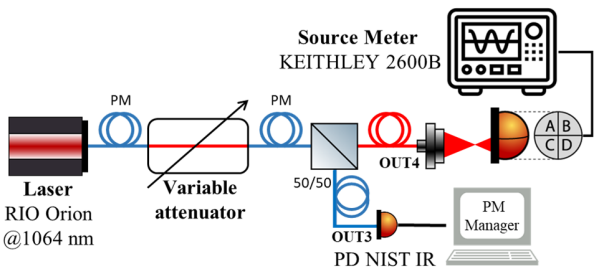

Fig. 1. Diagram of the experimental setup for responsivity measurement.

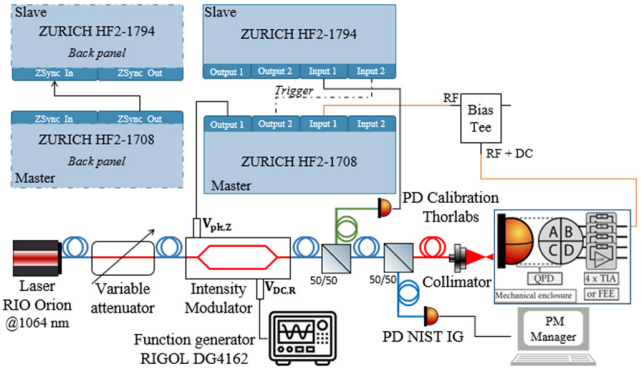

Fig. 2. Diagram of the experimental setup for measuring QPR phase and amplitude response to ac LISA-like signals.

the Netherlands (NL) [6] and Japan (JP). The current version of the TIA is designed by Germany (DE) [7]. For optimal operation, the standard bias voltage is set at 20 V for NL QPDs and 5 V for JP QPDs, both levels ensuring full depletion of the devices. To validate LISA specifications, the QPD must demonstrate a dark current <1 μA, a responsivity >0.7 A/W, and a 1.5-mm diameter active area, enhancing the sensitivity of the detector and improving the alignment. Once connected to the FEE, the equivalent input current noise of the QPR must be maintained below 2 pA/$\sqrt{\text{Hz}}$ over the LISA heterodyne frequency range from 3 to 28 MHz. The operational temperature range for LISA is between $+10$ °C and $+30$ °C.

B. Experimental Setup and Procedure Description

Dark current and capacitance measurements of the QPDs are carried out using a Keithley 4200 Semiconductor Characterization System (SCS). The QPD is placed in a temperature-controlled copper support which is housed in a metallic enclosure to ensure darkness. The temperature system is a Peltier cooler regulated with a thermoelectric controller (TEC) and monitored using a temperature probe. Dark current is simultaneously measured on all quadrants with the same reverse bias voltage applied to each quadrant at different temperatures between 20 °C and 50 °C. Temperatures below 20 °C were not performed due to condensation appearing and compromising the integrity of the QPD. The voltage sweep is conducted from 0 to 30 V in 1-V steps for NL QPDs and from -0.25 to 6 V in 0.25-V steps for JP QPDs. The capacitance of each quadrant is measured individually at 25 °C and with a voltage sweep-like dark current measurement and a frequency sweep of 1–10 MHz. The internal offset capacitance and current from the setup (cable and instruments) are subtracted from the final result. The experimental setup precision is estimated to be $\pm 4.1\%$ for dark current and $\pm 4.4\%$ for capacitance.

The responsivity represents the ratio of photocurrent to optical power in a photodiode (PD). It is quantified using the setup shown in Fig. 1. A 1064-nm continuous laser beam, emitted by a fiber-coupled laser source, is focused onto a QPD quadrant using a collimator. The laser beam's shape and size are calibrated using a Thorlabs beam profiler. The beam's optical power is tracked using an NIST InGaAs PD, and the QPD photocurrent is measured using a Keithley 2600B source meter. The setup's estimated error is $\pm 3\%$.

After being connected to the FEE, QPRs undergo equivalent input current noise measurements for each channel using the "white light method" detailed in [8] and [9]. These references report the same experimental setup, except that we additionally measure the noise floor of the measurement chain, alongside the spectral noise in dark and light conditions using a Rohde and Schwarz FSP13 spectrum analyzer. The setup precision is estimated to be $\pm 5\%$ in the LISA bandwidth frequency range (3–30 MHz) and $\pm 20\%$ in the high-frequency range (>40 MHz).

The LISA mission employs three interferometers: long arm, test mass, and reference. Each LISA interferometric optical signal, denoted by $S(t)^{\text{HET}}$, is modelized by (1). This equation described the interaction of two coherent laser beams, characterized by their optical powers $P1$ and $P2$, a phase difference $\varphi_r(t)$ between the beams, and the efficiency η_e of the heterodyne interferometer

$$S(t)^{\text{HET}} = \frac{P_1 + P_2}{2} + \sqrt{\eta_e P_1 P_2}\sin(\varphi_r(t)). \tag{1}$$

To accurately reproduce each LISA interferometer, our experimental setup, illustrated in Fig. 2, employs an intensity modulator controlled with a Zurich lock-in amplifier [10]. The output signal is monitored using two PDs, an NIST PD for the dc optical signal and a Thorlabs calibrated PD with a 1.2-GHz bandwidth for the ac signal. The laser beam is focused on a single QPD segment. The amplitude and phase responses of the illuminated QPR channel are observed relative to an optical power sweep from 0 to 110 μW, and a frequency sweep from 0 to 30 MHz representative of LISA optical power and bandwidth. This test was performed only on four QPDs: two NL QPDs and two JP QPDs, each with a diameter of 1.5 mm, with one from each set serving as a reference and the other used for irradiation.

C. LISA Radiation Environment and Specification

During an extended 12.5-year mission, LISA will face exposure to various radiation types, such as solar wind, solar flares, and cosmic radiation [11]. Energetic particles from these sources penetrate the spacecraft walls and interact with matter through the atomic electron cloud or nuclei. The former interaction can ionize atoms, creating electron–hole pairs, and

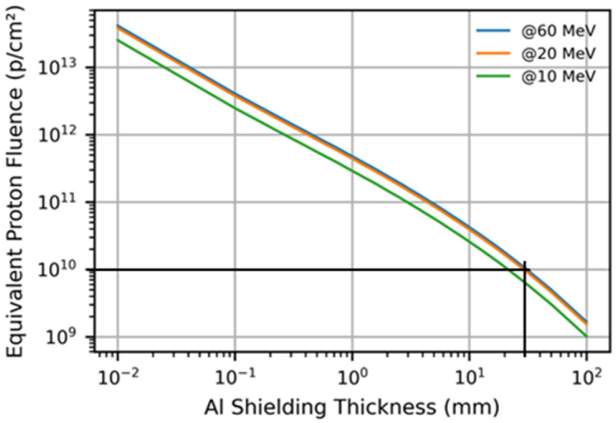

Fig. 3. OMERE proton equivalent fluence for LISA's 12.5-year lifetime at 10, 20, and 60 MeV versus Al shield thickness. LISA's estimated shield thickness for the QPR is 3 mm.

resulting in a cumulative effect known as total ionizing dose (TID), measured by linear energy transfer (LET). The latter interaction can eject nuclei, causing vacancies and interstitials in the semiconductor lattice, a process known as atomic displacement damage. This process is quantified by the non-ionizing energy loss (NIEL) and displacement damage dose (DDD). Both NIEL and LET are defined for specific energy particles in a given material. Crystal defects from ionizing or displacement damage introduce parasitic levels in the semiconductor bandgap, leading to electron–hole pair generation, recombination, carrier trapping, dopant compensation, and tunneling effects. These phenomena degrade semiconductor properties, and therefore, the QPD by increasing dark current, reducing carrier lifetime and mobility, and altering carrier concentration and conductivity [12], [13], [14], [15], [16], [17].

In the LISA orbit, solar flare events constitute the primary radiation challenge. For a 12.5-year mission with a 3-mm aluminum shield, ESA's worst-case scenario requirements for the optical bench components include a TID of 40 krad (InGaAs) and a displacement damage equivalent fluence (DDEF) of $1.01 \times 10^{+11}$ p/cm^2 for 10-MeV protons, corresponding to a DDD of $6.62 \times 10^{+8}$ MeV/g (InGaAs) [11], [18]. Using the mission's cumulative fluence from the NASA GSFC ESP model [19] and the InGaAs NIEL data from NEMO [20], it is possible to use the software OMERE [21] to calculate the 10-MeV proton equivalent fluence, yielding results consistent with the original DDEF. Additionally depicted in Fig. 3, OMERE provides the DDEF for 20- and 60-MeV energies, important for proton irradiation.

D. Irradiation Plan and Conditions

The QPD underwent three irradiation campaigns. Table I outlines the number of NL and JP QPDs irradiated for each irradiation under protons, electrons, and gamma rays.

Table II shows the exposure conditions for all irradiation campaigns at the last fluence step. The TID is simply the product of the applied fluence by the electronic stopping power of the particles provided by SRIM [22] for protons and ESTAR [23] for electrons. Similarly, the DDD is the product of the applied fluence by the NIEL calculated with NEMO [20]. DDD values were determined by multiplying the NIEL values obtained from SR-NIEL [24] for InGaAs by the fluence applied to the QPDs.

Achieving the final fluence involved multiple steps, as detailed in Table III. At each step, only measurements for capacitance at 25 °C, dark current at 20 °C, 35 °C, and 50 °C, as well as QPR equivalent input current noise were recorded.

TABLE I
IRRADIATION QPD AND ORGANIZATION

Type	Energy (MeV)	Total Number of QPDs	QPD Origin	QPD Size
Protons (CAL)	20	3	JP	1, 1.5, 2 mm
		1	NL	1.5 mm
	60	3	JP	1, 1.5, 2 mm
		1	NL	1.5 mm
Electrons (ONERA)	0.5	2	JP	1 & 2 mm
	1	3	JP	1, 1.5, 2 mm
Gamma (ONERA)	1.25	1	JP	1.5 mm
		1	NL	1.5 mm

TABLE II
TID AND DDD APPLIED ON A QPD FOR ALL IRRADIATIONS

Particle type	Energy (MeV)	Fluence (p/cm²)	TID (krad)	DDD (MeV/g)
Proton (CAL)	20	$1.0\text{x}10^{+12}$	237	$4.8\text{x}10^{+9}$
	60	$1.0\text{x}10^{+12}$	104	$3.6\text{x}10^{+9}$
Electron (ONERA)	0.5	$5.0\text{x}10^{+12}$	105	$3.36\text{x}10^{+7}$
	1.0	$5.0\text{x}10^{+12}$	100	$9.71\text{x}10^{+7}$
Gamma (ONERA)	1.25		237	$\sim 10^{+7}$

TABLE III
CUMULATIVE FLUENCE AND DOSE TABLE FOR PROTONS, ELECTRONS, AND GAMMA RADIATION AT EACH IRRADIATION STEP

Proton Cumulative Fluence (p/cm²)		Electron Cumulative Fluence (e/cm²)	Gamma Cumulative Dose (krad)
60 MeV	20 MeV	0.5 & 1.0 MeV	1.25 MeV
$2.0\text{x}10^{+9}$	$2.0\text{x}10^{+9}$	$0.5\text{x}10^{+12}$	1
$4.0\text{x}10^{+9}$	$4.0\text{x}10^{+9}$	$1.0\text{x}10^{+12}$	2
$8.4\text{x}10^{+9}$	$8.4\text{x}10^{+9}$	$2.0\text{x}10^{+12}$	22
$4.2\text{x}10^{+10}$	$2.1\text{x}10^{+11}$	$3.0\text{x}10^{+12}$	36
$2.1\text{x}10^{+11}$	$1.0\text{x}10^{+12}$	$4.0\text{x}10^{+12}$	108
$1.0\text{x}10^{+12}$		$5.0\text{x}10^{+12}$	150
			237

E. Irradiation Facilities

Proton irradiation was carried out using the MEDICYC Research and Development line at the CAL in Nice, France [25]. The facility hosts a 65-MeV isochronous cyclotron which delivers a 10-cm diameter beam with a beam homogeneity of less than ±3%.

Electron irradiation was performed at ONERA (Toulouse, France) in the MIRAGE facility. A 2-MeV electron Van de Graaff accelerator generates the beam. Beam flux was measured with a Faraday cup, ensuring an overall homogeneity

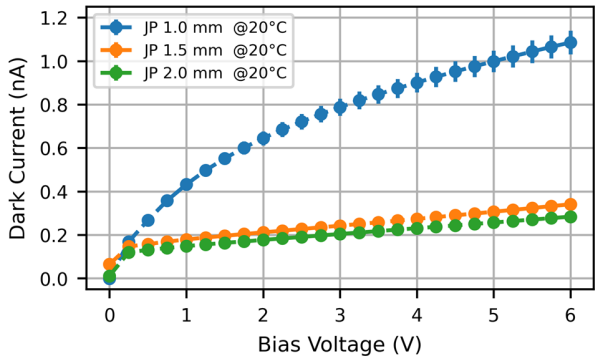

Fig. 4. Dark current for JP QPDs at 20 °C versus the reverse bias voltage. Error bars correspond to the estimated measurement precision.

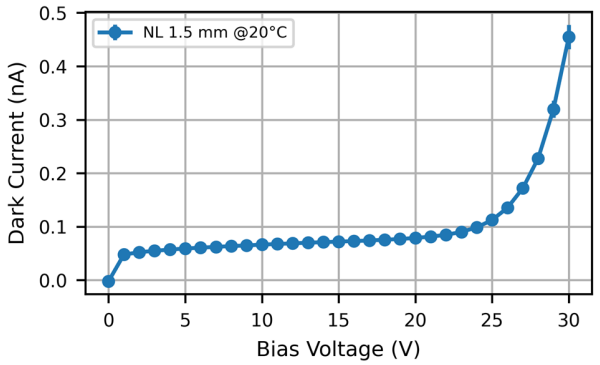

Fig. 5. Dark current for NL QPD at 20 °C versus the reverse bias voltage. Error bars correspond to the estimated measurement precision.

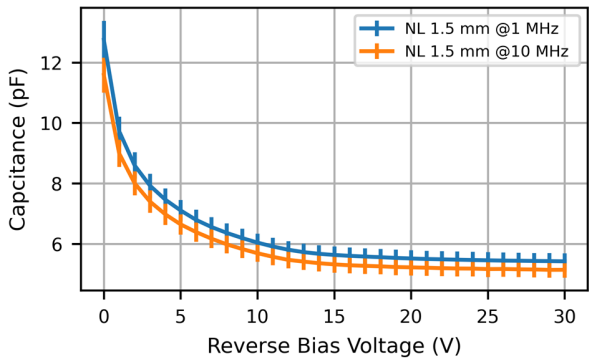

Fig. 6. Capacitance for NL QPD at 1 and 10 MHz versus the reverse bias voltage. Error bars correspond to the estimated measurement precision.

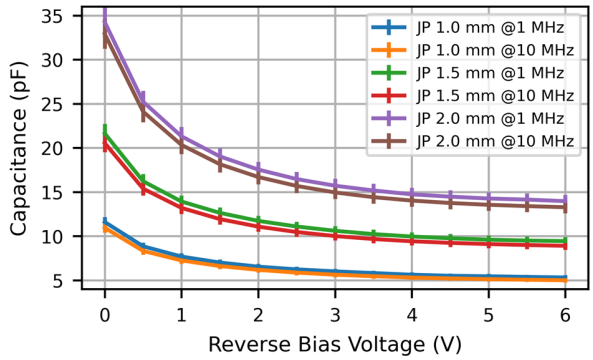

Fig. 7. Capacitance for JP QPDs at 1 and 10 MHz versus the reverse bias voltage. Error bars correspond to the estimated measurement precision.

and accuracy of ±10%. Samples were placed under a vacuum of 10^{-6}–10^{-7} mbar.

Gamma-ray irradiation was also conducted at ONERA, using the Co^{60} MEGA facility. The dosimetry was performed with ionization chambers, achieving an overall accuracy of ±10%.

III. Data Result and Analysis

This section outlines the QPDs evaluations for each parameter outlined in Section II, across pre-irradiation, in situ, and post-irradiation phases. Experimental findings indicate consistent results across all four segments of the QPD and QPR channels tested (named respectively, segments A–D and channels A–D). Therefore, as a rule of thumb, only one segment per QPD or one channel per QPR type is depicted in all figures throughout this article.

A. Pre-Irradiation Results

The dark current for all QPDs varied from 80 pA to 1.1 nA at 20 °C, as illustrated in Figs. 4 and 5. The highest dark current was measured at 4 nA for a 2.0-mm diameter JP QPD at 50 °C. Capacitance measurements for both JP and NL QPDs, conducted at two frequencies, are depicted in Figs. 6 and 7.

Pre-irradiation responsivity results indicate values up to 0.83 A/W, surpassing the LISA requirement of 0.70 A/W.

The noise levels in the LISA QPR for JP QPDs of each diameter and NL QPDs are illustrated in Fig. 8. QPDs with capacitance below 6 pF, remain within LISA's threshold of 2 pA/$\sqrt{\text{Hz}}$ in the range of 3–28-MHz.

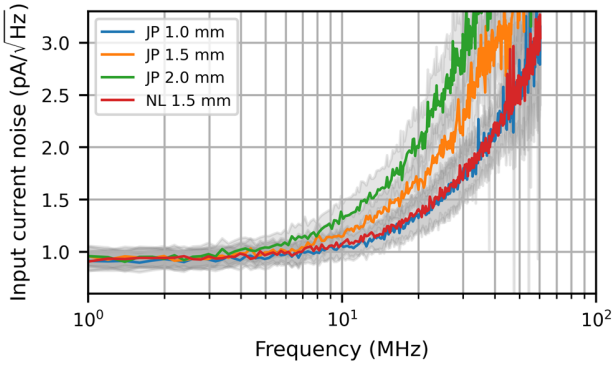

Fig. 8. Equivalent input current noise for JP and NL QPD versus the frequency. The gray zone represents the estimated measurement precision.

B. Irradiation Results

In response to fluences from protons and electrons, as well as gamma rays, there is a marked increase in the dark current observed in both JP and NL QPDs. This trend is displayed in Figs. 9–12, which display the dark current results conducted on-site following each irradiation step. Error bars correspond to the estimated measurement error. Figs. 9 and 10 detail the response to proton irradiation, Fig. 11 illustrates the impact of electron exposure, and Fig. 12 highlights the effects of gamma rays. The most pronounced increase was observed with

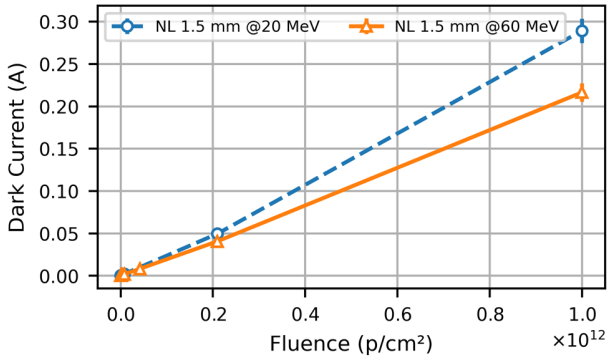

Fig. 9. Dark current measured at 20 °C and V_{bias} of 20 V for NL QPDs irradiated under 20- and 60-MeV protons versus the applied fluence.

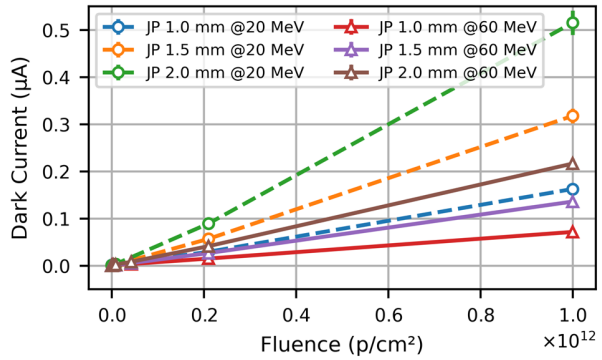

Fig. 10. Dark current measured at 20 °C and V_{bias} of 5 V for JP QPDs irradiated under 20- and 60-MeV protons versus the applied fluence.

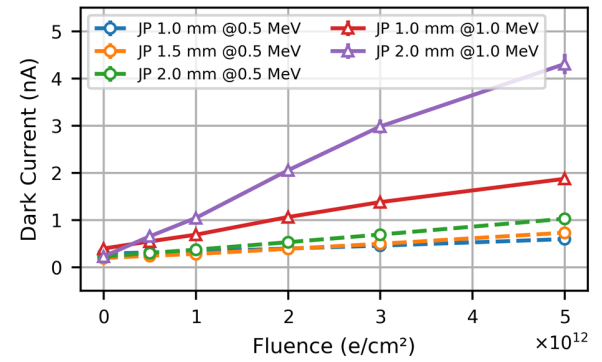

Fig. 11. Dark current measured at 20 °C and V_{bias} of 5 V for JP QPDs irradiated under 0.5- and 1.0-MeV electrons versus the applied fluence.

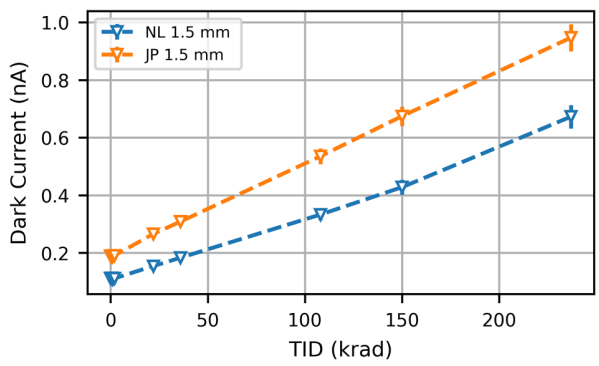

Fig. 12. Dark current measured at 20 °C and V_{bias} of 20 V for 1.5-mm JP and NL QPD irradiated under gamma rays versus the TID.

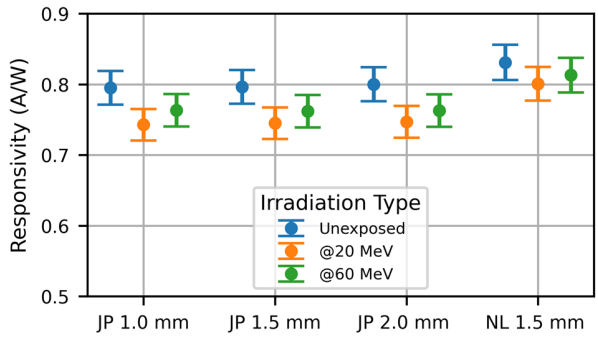

Fig. 13. Responsivity of unexposed and irradiated JP and NL QPDs under 20- and 60-MeV protons at a final fluence of $1 \times 10^{+12}$ p/cm^2. Errors bars represent the estimated measurement error.

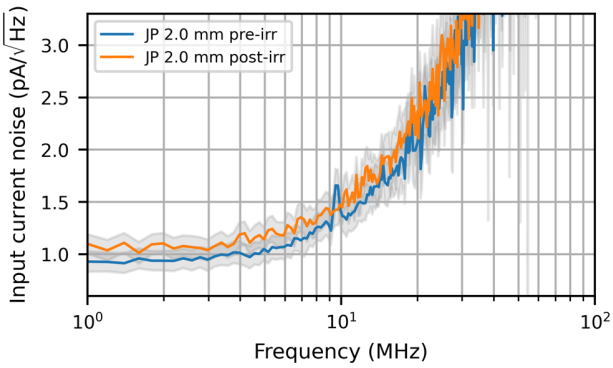

Fig. 14. Equivalent input current noise of the 2.0-mm JP QPD pre and post-20-MeV protons irradiation (fluence of $1 \times 10^{+12}$ p/cm^2) versus the frequency. The gray zone represents the estimated measurement precision.

20-MeV protons for the 2.0-mm diameter QPD, registering a maximum of 0.5 μA at 20 °C and reaching up to 4.4 μA at 50 °C. However, under the LISA-required fluence condition for proton irradiation of $1.41 \times 10^{+11}$ p/cm^2 at 20 MeV and temperature below 30 °C, all QPDs successfully kept their dark current levels below the LISA threshold of 1.0 μA. In contrast to dark current, no notable changes in capacitance for all QPD were observed.

Neither electron nor gamma-ray irradiation led to any measurable changes in responsivity. In Fig. 13, a decrease in the QPD responsivity can be noted for proton irradiation with a maximum of ∼9% and ∼5% for, respectively, JP and NL QPD at 20 MeV. However, even at a fluence level of $1 \times 10^{+12}$ p/cm^2, the responsivity remained above the LISA requirement of 0.7 A/W. The drop in responsivity following proton irradiation was more significant at 20 MeV, approximately 1.7 times higher than at 60 MeV. It is important to note that the data in Fig. 13 were taken six months after the proton irradiation campaign.

Mirroring the approach in [26], [27], [28], and [29], irradiated QPDs connected to nonirradiated FEE, exhibited consistent QPR noise levels pre- and post-irradiation, except for only the 2.0-mm diameter QPD irradiated with 20-MeV protons, as illustrated in Fig. 14. This QPD showed a 0.16-pA/$\sqrt{\text{Hz}}$ noise increase and a 2.0-MHz bandwidth decrease. This behavior likely results from the current shot noise density $I_{\text{shot}}(f)$ affecting the QPR equivalent input

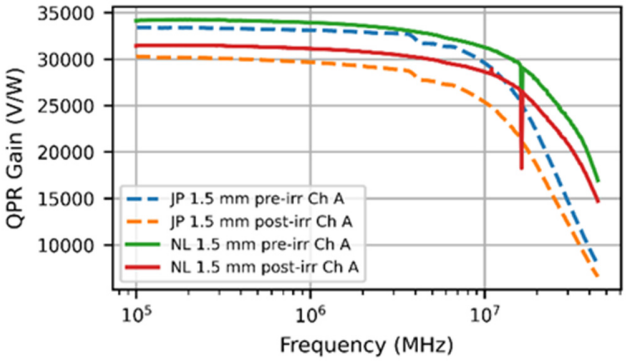

Fig. 15. QPR Gain for 1.5-mm NL QPD and 1.5-mm JP QPD pre and post-20-MeV protons irradiation (cumulated fluence of $1 \times 10^{+12}$ p/cm^2) versus the frequency.

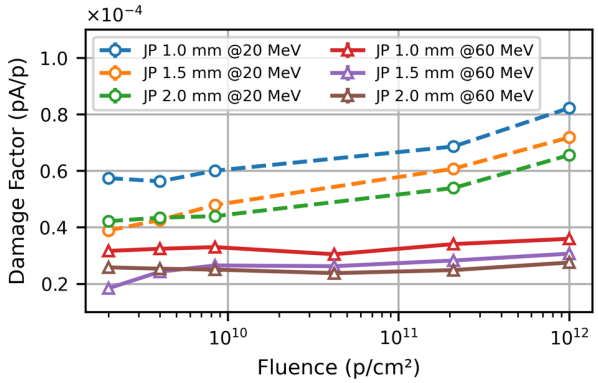

Fig. 16. Damage factor from dark current measurement at V_{bias} of 5 V and at 20 °C of JP QPDs irradiated under 20- and 60-MeV protons versus applied fluence.

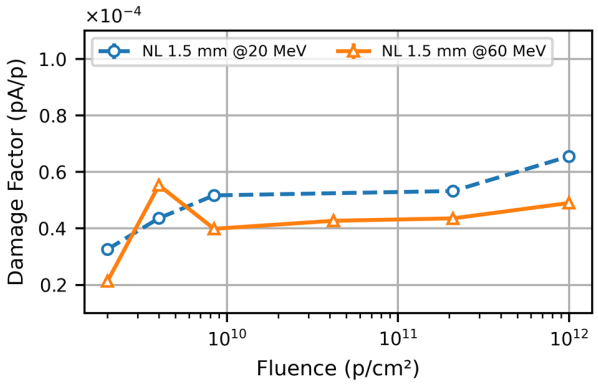

Fig. 17. Damage factor from dark current measurement at V_{bias} of 20 V and at 20 °C of NL QPDs irradiated under 20- and 60-MeV protons versus applied fluence.

current noise, determined by both the photocurrent I_{ph} (A) and the dark current I_{dark} (A), as detailed in the following equation [27], [28], [29], [30]:

$$I_{\text{shot}}(f) = \sqrt{2e\left[I_{\text{ph}} + I_{\text{dark}}\right]}, \quad (\text{A}/\sqrt{\text{Hz}}) \tag{2}$$

where f is the frequency (Hz) and e is the elementary charge (C).

The drop in responsivity previously seen in Fig. 13, leads to a corresponding reduction in the QPR amplitude response of about ∼9% for JP QPD and 6% for NL QPD as depicted in Fig. 15. Notably, while the amplitude response is affected, the signal's phase remains consistent for both JP and NL QPDs.

IV. Damage Factor and Discussion

A. Dark Current Damage Factor

The damage factor ($K_{I\text{dark}}$) is regularly used to compare, evaluate, and predict the radiation tolerance of various devices or semiconductors [12], [14], [31], [32], [33], [34], [35], [36], [37], [38] and is described by the following equation based on the definition given by [13], [16], and [39]:

$$K_{I\text{dark}} = \frac{I_{\text{dark}}(\Phi) - I_{\text{dark}}(0)}{\Phi \cdot S} \tag{3}$$

where $I_{\text{dark}}(\Phi)$ is the dark current measured at the fluence Φ, $I_{\text{dark}}(0)$ is the dark current measured prior irradiation, and S is the area surface of one QPD's segment.

The damage factor, integrating both ionizing and nonionizing effects [36], may lead to inaccuracies when compared directly with the NIEL. Gamma-ray radiation is used as a benchmark to evaluate the maximal ionizing contribution for proton and electron irradiation, using the strong assumption that the dark current increase in gamma radiation is only due to ionizing damage. This approach allows us to consider the worst case. According to Figs. 10–12, the dark current increase for protons at a TID of 237 krad is approximately 0.3 μA, in contrast to less than 1 nA for gamma irradiation under identical QPD type and TID conditions. Thus, the ionizing contribution for protons (<1%) is considered negligible. On the other hand, electron irradiation results in a 550 pA increase in dark current at a TID of 105 krad for a 1.5-mm JP QPD versus a 350 pA increase from gamma irradiation. This suggests that in the worst-case scenario, ionizing damage from electron irradiation could account for up to 60% of the damage observed. Hence, the impact of ionization damage could be significant and cannot be neglected as for proton, potentially resulting in an overestimation of displacement damage assessments. However, the LET curve for electrons in InGaAs decreases from 500 keV to 1.0 MeV and Fig. 11 reveals a higher increase in dark current at 1.0 MeV compared with 0.5 MeV, suggesting displacement damage predominates over ionizing damage. Nevertheless, precisely quantifying displacement damage's exact contribution continues to pose a significant challenge.

In Figs. 16–18, damage factors were plotted as a function of the fluence for QPDs exposed to proton irradiation at 20 and 60 MeV, and electron irradiation at 0.5 and 1.0 MeV. Damage factors were computed for all irradiation steps, with fluence levels detailed in Table III. For 60-MeV proton irradiation, the damage factor showed relative stability, with an average increase of around 19% from the initial to the final steps. In contrast, QPDs irradiated at 20 MeV exhibited a more substantial increase, around 50%. Ideally, damage factors should remain consistent regardless of fluence levels. While statistical effects can cause an increase in damage factor with fluence [40], [41], this study's focus on large-diameter QPDs indicates such fluctuations are more prominent at lower fluence

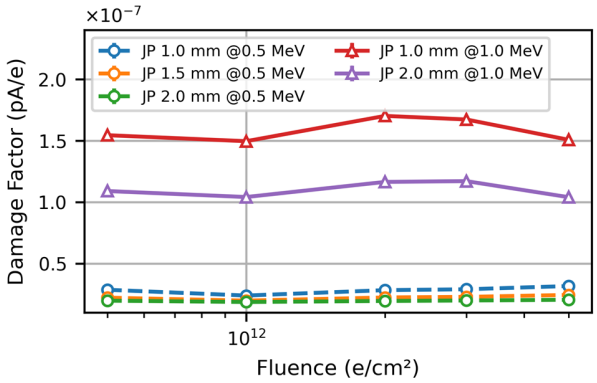

Fig. 18. Damage factor from dark current measurement at V_{bias} of 5 V and at 20 °C of JP QPDs irradiated under 0.5- and 1.0-MeV electrons versus applied fluence.

TABLE IV

$K_{I\text{DARK}}$ FROM THE LITERATURE OF INGAAS PDS IRRADIATED UNDER PROTONS

Ref	Devices	Energy (MeV)	Fluence (p/cm²)	K_{Idark} (pA/p)
[16]	FCIQ1000	60	$1.0\text{x}10^{+12}$	$3.62\text{x}10^{-4}$
	C30168		$3.0\text{x}10^{+11}$	$7.55\text{x}10^{-4}$
[42]	G8195	60	$1.0\text{x}10^{+12}$	$2.74\text{x}10^{-4}$
	PM1R		$1.0\text{x}10^{+12}$	$1.98\text{x}10^{-4}$
	GAP394		$1.0\text{x}10^{+12}$	$2.98\text{x}10^{-4}$
	EPM605LL		$1.0\text{x}10^{+12}$	$6.76\text{x}10^{-4}$
	HRS		$1.3\text{x}10^{+11}$	$3.95\text{x}10^{-4}$
	C30168		$3.0\text{x}10^{+11}$	$8.07\text{x}10^{-4}$
[43]	Cactus	49.3	$3.0\text{x}10^{+11}$	$1.70\text{x}10^{-3}$
[29]	1.0 mm QPD	30	$2.3\text{x}10^{+11}$	$3.82\text{x}10^{-5}$
	2.0 mm QPD		$2.3\text{x}10^{+11}$	$3.98\text{x}10^{-5}$

levels, below $1 \times 10^{+12}$ p/cm^2 [41] suggesting a different cause. Conversely, for electron irradiation, the damage factor remained stable.

Table IV summarizes the damage factors from previous studies [16], [29], [42], [43]. In [29], the damage factors were derived using the damage factor formula from (3) and the dark current results reported in this article. Compared with [16], [42], and [43], the damage factors presented in Figs. 16 and 17 are notably lower by a factor of at least 5.

These discrepancies may be attributed to the potential use of dual depletion region (DDR) QPD technology [28], [29] in JP and NL QPDs. Indeed, Joshi and Datta [29] utilized DDR QPDs reported values close to ours. In addition, these discrepancies might be due to the impact of doping levels on the damage factor [44]. The QPDs used here have low doping levels, below $1 \times 10^{+14}$ cm^{-3}, 70 times lower than those in [43].

B. NIEL Scaling Approach

The NIEL scaling approach, founded on the linear relationship between the NIEL and the dark current damage factor, provides a framework for estimating and predicting radiation damage in semiconductor devices. It applies the concept that the impact of radiation can be scaled based on the NIEL, allowing for more accurate predictions of device behavior

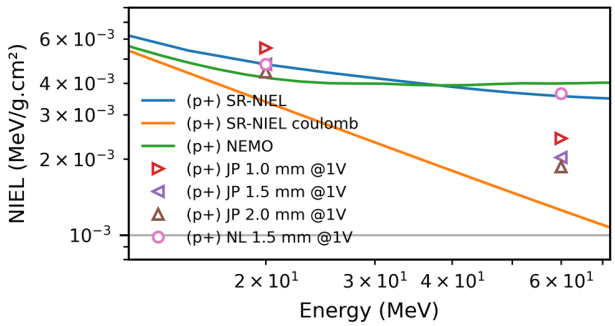

Fig. 19. Comparison between the NIEL spectra and dark current damage factor from proton irradiation. NIEL calculation performed with NEMO and SR-NIEL with $E_d = 15$ eV for In and 10 eV for Ga and As.

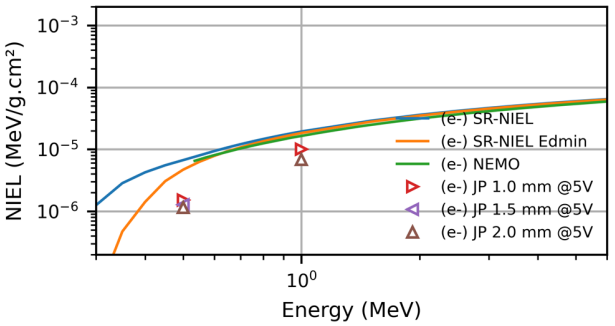

Fig. 20. Comparison between the NIEL spectra and dark current damage factor from electron irradiation. NIEL calculation performed with SR-NIEL and NEMO with $E_d = 15$ eV for In and 10 eV for Ga and As. E_d for SR-NIEL Edmin is based on $E_{d\text{min}}$ from [47].

under various radiation conditions [12], [13], [14], [16], [31], [32], [33], [34], [35], [37], [38], [39], [41], [42], [45], [46].

NIEL values for protons were calculated using both NEMO [20] and SR-NIEL [24] software, employing displacement thresholds of 15 eV for indium and 10 eV for gallium and Arsenic, which align with prior research [42]. In addition, NIEL was computed using the more recent threshold value $E_{d\text{min}}$ from [47]. Fig. 19 presents the NIEL results from both SR-NIEL and NEMO, encompassing a total NIEL which includes Coulombic and Hadronic contributions. Fig. 19 also displays normalized experimental damage factors for JP and NL QPDs, plotted against incident particle energy, in conjunction with their corresponding NIEL values. The scaling factor used was for JP QPDs 1.49×10^{-14} A · g/MeV/cm^2 and for NL QPDs 1.38×10^{-14}A · g/MeV/cm^2. While the data for NL QPDs align with the general NIEL trend, the JP QPDs exhibit a distinct behavior, matching more with the Coulombic NIEL predictions. This deviation is mirrored for one InGaAs device (1931SGN detectors) discussed in [42], where the damage factor ratio is ∼2, like the JP QPDs. In contrast, a ratio of ∼1.3 is observed for NL QPDs and similar for detectors like PD7006 and the Spot 4 MIR cited in [42].

Fig. 20 represents the results from electron irradiation using the same NIEL scaling approach as previously used for proton irradiation. A notable deviation from the NIEL values for low-energy electrons is evident, consistent with findings in [35] and [36].

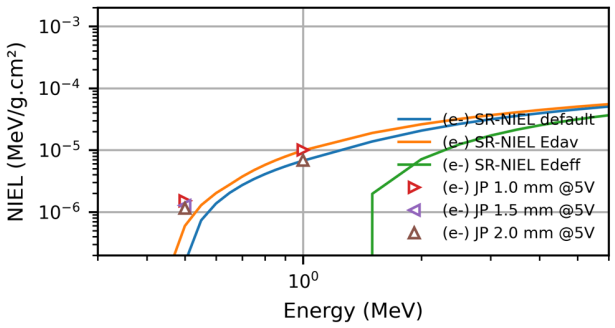

Fig. 21. Comparison between the NIEL spectra and dark current damage factor from electron irradiation. NIEL calculations performed with SR-NIEL with E_d for E_{dav} and E_{deff} from [47] and from SR-NIEL [37], [38] for default.

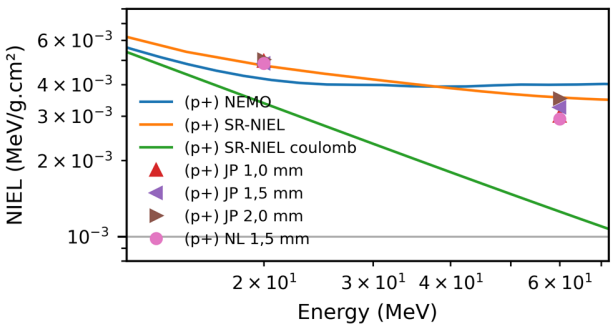

Fig. 22. Comparison between the NIEL spectra and responsivity damage factor from proton irradiation. NIEL calculation performed with NEMO and SR-NIEL with $E_d = 15$ eV for In and 10 eV for Ga and As.

In Fig. 21, our data match also with new values of NIEL obtained using SR-NIEL and new threshold displacement energy from experimental data [37], [38], [47]. Precisely, in Fig. 21, E_{dav} and E_{deff} are from [47] and "SR-NIEL default" values correspond to the default threshold from SR-NIEL, derived from experimental data on irradiated solar cells [37], [38]. This suggests that the discrepancy regarding the NIEL for electron and experimental data is not limited just our study.

These experimental deviations to the NIEL are interpreted by references [48], [49], [50], which suggest that the traditional model predicated by a sudden onset of atom ejection beyond a specific energy threshold may not accurately describe low-energy interactions. Molecular dynamics simulations propose a gradual change in atom ejection probability. When it comes to low-energy electrons that generate numerous low-energy PKA or primary knock-on-atom, the classic model could substantially overstate NIEL values.

C. NIEL Scaling Approach Applied for Responsivity Result

The NIEL scaling approach was applied to the responsivity results using the same methodology as that for the dark current. Therefore, the damage factor for responsivity K_R, is defined by the following eequation:

$$K_R = -\frac{R(\Phi) - R(0)}{\Phi} \tag{4}$$

where $R(\Phi)$ represents the responsivity of the QPD measured at the fluence Φ and $R(0)$ represents the responsivity measured before irradiation. Fig. 22 shows a deviation from the previous NIEL curve in Fig. 19, obtained from dark current results. This difference may be due to several factors: the antireflective layer on the QPDs, the precision of the responsivity measurement, and different annealing rates between NL and JP QPDs since the post-irradiation measurements took place six months after the irradiation campaign.

D. Influence of the Electric Fields on the Damage Factor

Figs. 23 and 24 illustrate the damage factor derived from dark current in JP and NL QPDs irradiated with 20- and 60-MeV protons, plotted against reverse bias voltage. These figures suggest that the bias voltage influences the damage factor, aligning with the phenomena in [43], where the electric field intensifies thermal carrier generation in InGaAs PDs

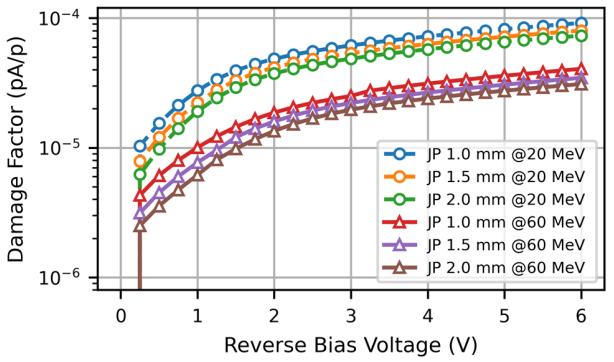

Fig. 23. Damage factor from dark current measurement at 20 °C of JP QPDs irradiated under 20- and 60-MeV protons at the last fluence step of $1 \times 10^{+12}$ p/cm^2 versus the reverse bias voltage.

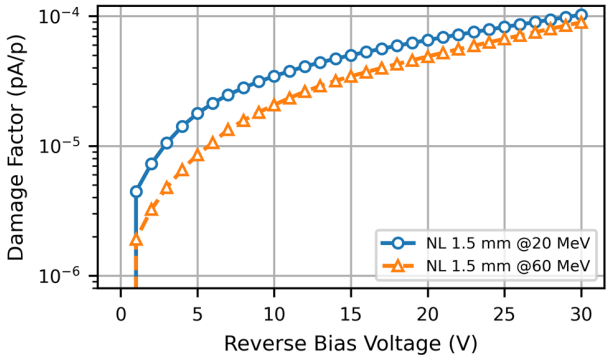

Fig. 24. Damage factor from dark current measurement at 20 °C of NL QPDs irradiated under 20- and 60-MeV protons at the last fluence step of $1 \times 10^{+12}$ p/cm^2 versus the reverse bias voltage.

due to Shockley–Read–Hall generation centers. To minimize the consequences due to radiation, a low reverse bias is recommended for space applications.

From dark current measurements, the activation energy (E_a) was calculated for 1.5-mm JP and NL from the Arrhenius law

$$I = Ae^{-\frac{E_a}{kT}} \tag{5}$$

where A is a prefactor, k is Boltzmann's constant, and T is the temperature. The E_a values are the average across all four channels. Distinct behaviors were observed. JP QPDs irradiated under 20-MeV protons at a V_{bias} of 5 V exhibit minimal changes in E_a, varying from 0.63 to 0.58 eV after irradiation, with similar results for QPDs

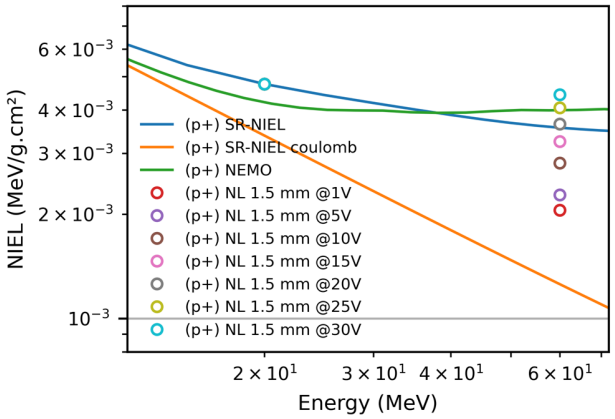

Fig. 25. Comparison between the NIEL spectra and 1.5-mm NL QPDs dark current damage factor from proton irradiation at different bias voltages.

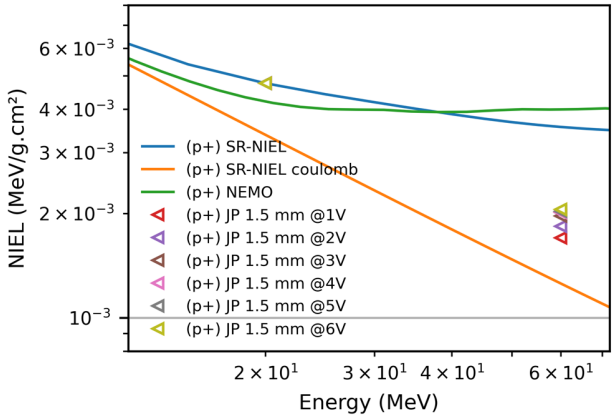

Fig. 26. Comparison between the NIEL spectra and 1.5-mm JP QPDs dark current damage factor from proton irradiation at different bias voltages.

under 60-MeV protons. This observation indicates a sustained generation–recombination mechanism. In contrast, the NL QPDs irradiated under 20 MeV at a V_{bias} of 20 V, experienced a significant E_a shift from 0.79 to 0.49 eV after irradiation, with similar results for NL QPDs under 60-MeV protons. This observation indicates a shift from diffusion limited to generation–recombination-dominated dark current, as also observed in [43], where the electric field effects intensify carrier generation in irradiated InGaAs QPDs. Those two behaviors can also be found in [42] with 1931SGM and G8195 detectors. The activation energy was observed to decrease with increased reverse bias. Pre-irradiation JP QPDs show a variation of E_a from 0.7 eV at 1 V to 0.60 eV at 5 V and for NL QPDs from 0.85 eV at 1 V to 0.55 eV at 30 V. Similar observations to NL QPDs are reported in [43], where E_a decreased with the reverse bias with a range from approximately 0.88–0.58 eV. However, our study's limitations must be acknowledged. The absence of detailed data on depletion thickness, exact doping levels, and electric field profiles prevents a full comparison with [42] and [43]. Future work will focus on this point.

This dependence also impacts the NIEL scaling approach, as illustrated in Figs. 25 and 26 and [51]. The range of these factors extends from the Coulombic component at the lowest bias to the total NIEL at the highest. This variation is likely influenced by the electric field's magnitude in the depleted region, where defects were created during irradiation. However, a definitive explanation for this behavior remains to be established.

V. Conclusion

The InGaAs QPDs have showcased robust radiation tolerance, with no breakdown under various radiation types, such as proton, electron, and gamma rays. Their resilience was confirmed up to a TID of 237 krad and a DDD of $4.8 \times 10^{+9}$ MeV/g. Dark currents exhibited a consistent rise, peaking at $\sim$0.5 μA for the 2-mm JP QPD under 20-MeV proton irradiation at 20 °C but remained within LISA's specifications. While capacitance and noise largely remained unchanged, a 0.16-pA/$\sqrt{\text{Hz}}$ uptick was seen in the same 2-mm QPD post-20-MeV irradiation, likely due to the rise in dark current. Even with a maximum responsivity drop of $\sim$9%, the levels still exceed LISA's 0.7-A/W requirement, reaffirming QPDs' suitability for space applications like LISA.

The damage factors derived from both proton and electron results exhibit distinct behaviors. While the proton-induced damage aligns with the total NIEL predictions obtained from the SR-NIEL software, electron-induced damage indicates potential inaccuracies in traditional models at low energies. In addition, our study and works [43], [51] highlight the electric field impact on the damage factor and its role in the NIEL scaling approach.

Acknowledgment

The authors express their gratitude to the team at CAL, Nice, France, for their technical assistance during the proton irradiation and to Romain Rey for his technical support during electron irradiation at ONERA, Toulouse, France. They also extend their thanks to the ARTEMIS Laboratory, Observatories de la Côte d'Azur, Nice. In addition, they also acknowledge the laser interferometer space antenna (LISA) quadrant photoreceiver (QPR) working group for their support and insightful discussions. Their contributions have been invaluable in the development of this work.

References

[1] P. A. Seoane et al., "The gravitational universe," 2013, *arXiv:1305.5720*.
[2] J. Baker et al., "The laser interferometer space antenna: Unveiling the millihertz gravitational wave sky," 2019, *arXiv:1907.06482*.
[3] P. Amaro-Seoane et al., "Laser interferometer space antenna," 2017, *arXiv:1702.00786*.
[4] P. Amaro-Seoane et al., "Astrophysics with the laser interferometer space antenna," *Living Rev. Relativity*, vol. 26, no. 1, Mar. 2023, Art. no. 2, doi: 10.1007/s41114-022-00041-y.
[5] *Design Description LISA Payload Description Document Input*, ESA, Noordwijk, The Netherlands, 2017.
[6] J. I. Zand et al., "LISA QPR TRL6 design report," SRON, Leiden, The Netherlands, Tech. Rep. SRON-LISA-QPR-RP-001, Jul. 2023.
[7] G. F. Barranco and G. Heinzel, "A DC-coupled, HBT-based transimpedance amplifier for the LISA quadrant photoreceivers," *IEEE Trans. Aerosp. Electron. Syst.*, vol. 57, no. 5, pp. 2899–2904, Oct. 2021, doi: 10.1109/TAES.2021.3068437.
[8] G. F. Barranco, "Photodetection in intersatellite laser interferometers," Ph.D. dissertation, Dept. Fac. Elect. Eng. Comput. Sci., Univ. Gottfried Wilhelm Leibniz, Hanover, Germany, 2018.
[9] G. F. Barranco, "Characterization of LISA QPR FEEs prior to irradiation," Albert Einstein Inst., Hannover, Germany, Tech. Rep., 2021.

[10] S. Bruhier et al., "Design and characterization of quadrant photoreceivers for the AIVT of the LISA space instrument," Presented at the Optique, Nice, France, Jul. 2022. [Online]. Available: https://hal.science/hal-03772904v1/document

[11] M. Millinger and P. Jiggens, "LISA environment specification," ESA, Noordwijk, The Netherlands, Tech. Rep. ESA-L3-EST-MIS-SP-001, Jun. 2020.

[12] J. R. Srour, C. J. Marshall, and P. W. Marshall, "Review of displacement damage effects in silicon devices," *IEEE Trans. Nucl. Sci.*, vol. 50, no. 3, pp. 653–670, Jun. 2003, doi: 10.1109/TNS.2003.813197.

[13] J. R. Srour and J. W. Palko, "A framework for understanding displacement damage mechanisms in irradiated silicon devices," *IEEE Trans. Nucl. Sci.*, vol. 53, no. 6, pp. 3610–3620, Dec. 2006, doi: 10.1109/TNS.2006.885796.

[14] J. R. Srour and J. W. Palko, "Displacement damage effects in irradiated semiconductor devices," *IEEE Trans. Nucl. Sci.*, vol. 60, no. 3, pp. 1740–1766, Jun. 2013, doi: 10.1109/TNS.2013.2261316.

[15] P. Lantos, "The sun, the solar wind and their effects on the earth's environment," in *Space Radiation Environment and Its Effects on Spacecraft Components and Systems*, vol. 4. Toulouse, France: Cepadues, 2004, ch. 1-01, pp. 29–40.

[16] T. Nuns et al., "Displacement damage effects in InGaAs photodiodes due to electron, proton, and neutron irradiations," *IEEE Trans. Nucl. Sci.*, vol. 67, no. 7, pp. 1263–1272, Jul. 2020, doi: 10.1109/TNS.2020.2984133.

[17] G. R. Hopkinson, C. J. Dale, and P. W. Marshall, "Proton effects in charge-coupled devices," *IEEE Trans. Nucl. Sci.*, vol. 43, no. 2, pp. 614–627, Apr. 1996, doi: 10.1109/23.490905.

[18] N. Dinu-Jaeger, "LISA QPD irradiation tests report for TRA," OCA, Nice, France, Tests Tech. Rep. 1.0, May 2023.

[19] M. A. Xapsos, G. P. Summers, J. L. Barth, E. G. Stassinopoulos, and E. A. Burke, "Probability model for cumulative solar proton event fluences," *IEEE Trans. Nucl. Sci.*, vol. 47, no. 3, pp. 486–490, Jun. 2000, doi: 10.1109/23.856469.

[20] C. Inguimbert and R. Gigante, "NEMO: A code to compute NIEL of protons, neutrons, electrons, and heavy ions," *IEEE Trans. Nucl. Sci.*, vol. 53, no. 4, pp. 1967–1972, Aug. 2006, doi: 10.1109/TNS.2006.880926.

[21] (2023). *OMERE, Version 5.8.0, TRAD*. Accessed: Mar. 23, 2023. [Online]. Available: https://www.trad.fr/spatial/logiciel-omere/

[22] J. Ziegler. *SRIM & TRIM*. Accessed: Feb. 10, 2024. [Online]. Available: http://www.srim.org/

[23] *ESTAR*. Accessed: Feb. 10, 2024. [Online]. Available: https://physics.nist.gov/PhysRefData/Star/Text/ESTAR.html

[24] M. J. Boschini, P. G. Rancoita, and M. Tacconi. *SR-NIEL-7 Calculator: Screened Relativistic (SR) Treatment for Calculating the Displacement Damage and Nuclear Stopping Powers for Electrons, Protons, Light—And Heavy-Ions in Materials and Electronic Stopping Power*. Accessed: Dec. 8, 2023. [Online]. Available: https://www.sr-niel.org/

[25] P. Hofverberg et al., "A 60 MeV proton beam-line dedicated to research and development programs," *Appl. Radiat. Isot.*, vol. 184, Jun. 2022, Art. no. 110190, doi: 10.1016/j.apradiso.2022.110190.

[26] A. Joshi, F. Heine, and T. Feifel, "Rad-hard ultrafast InGaAs photodiodes for space applications," *Proc. SPIE*, vol. 6220, pp. 39–52, May 2006, doi: 10.1117/12.666055.

[27] A. Joshi, J. Rue, and S. Datta, "Low-noise large-area quad photoreceivers based on low-capacitance quad InGaAs photodiodes," *IEEE Photon. Technol. Lett.*, vol. 21, no. 21, pp. 1585–1587, Aug. 25, 2009, doi: 10.1109/LPT.2009.2030665.

[28] A. Joshi, S. Datta, J. Rue, J. Livas, R. Silverberg, and F. G. Cervantes, "Ultra-low noise large-area InGaAs quad photoreceiver with low crosstalk for laser interferometry space antenna," *Proc. SPIE*, vol. 8453, Sep. 2012, Art. no. 84532G, doi: 10.1117/12.918285.

[29] A. M. Joshi and S. Datta, "Space qualification of InGaAs photodiodes and photoreceivers," *Proc. SPIE*, vol. 10641, May 2018, Art. no. 106410K, doi: 10.1117/12.2304973.

[30] R. Alabedra and D. Rigaud, "Noise in photodiodes and photoreceiver systems," in *Optoelectronic Sensors*, D. Decoster and J. Harari, Eds. London, U.K.: ISTE, 2009, ch. 7, pp. 223–268, doi: 10.1002/9780470611630.ch7.

[31] G. P. Summers, E. A. Burke, C. J. Dale, E. A. Wolicki, P. W. Marshall, and M. A. Gehlhausen, "Correlation of particle-induced displacement damage in silicon," *IEEE Trans. Nucl. Sci.*, vol. NS-34, no. 6, pp. 1133–1139, Dec. 1987, doi: 10.1109/TNS.1987.4337442.

[32] G. P. Summers, E. A. Burke, P. Shapiro, S. R. Messenger, and R. J. Walters, "Damage correlations in semiconductors exposed to gamma, electron and proton radiations," *IEEE Trans. Nucl. Sci.*, vol. 40, no. 6, pp. 1372–1379, Dec. 1993, doi: 10.1109/23.273529.

[33] S. R. Messenger, R. J. Walters, E. A. Burke, G. P. Summers, and M. A. Xapsos, "NIEL and damage correlations for high-energy protons in gallium arsenide devices," *IEEE Trans. Nucl. Sci.*, vol. 48, no. 6, pp. 2121–2126, Dec. 2001, doi: 10.1109/23.983182.

[34] J. H. Warner et al., "Correlation of electron radiation induced-damage in GaAs solar cells," *IEEE Trans. Nucl. Sci.*, vol. 53, no. 4, pp. 1988–1994, Aug. 2006, doi: 10.1109/TNS.2006.877877.

[35] P. Arnolda, C. Inguimbert, T. Nuns, and C. Boatella-Polo, "NIEL scaling: Comparison with measured defect introduction rate in silicon," *IEEE Trans. Nucl. Sci.*, vol. 58, no. 3, pp. 756–763, Jun. 2011, doi: 10.1109/TNS.2011.2131154.

[36] T. Nuns, C. Inguimbert, S. Soonckindt, B. Dryer, T. Buggey, and C. Poivey, "Experimental study of the NIEL scaling for silicon devices," in *Proc. 18th Eur. Conf. Radiat. Effects Compon. Syst. (RADECS)*, Sep. 2018, pp. 1–8, doi: 10.1109/RADECS45761.2018.9328677.

[37] R. Campesato et al., "Effects of irradiation on triple and single junction InGaP/GaAs/Ge solar cells," in *Proc. 35th Eur. PV Solar Energy Conf.*, Brussels, Belgium, Sep. 2018, pp. 959–964.

[38] R. Campesato et al., "NIEL dose analysis on triple and single junction InGaP/GaAs/Ge solar cells irradiated with electrons, protons and neutrons," in *Proc. IEEE 46th Photovoltaic Specialists Conf. (PVSC)*, Chicago, IL, USA, Jun. 2019, pp. 2381–2384, doi: 10.1109/PVSC40753.2019.8980581.

[39] J. R. Srour and D. H. Lo, "Universal damage factor for radiation-induced dark current in silicon devices," *IEEE Trans. Nucl. Sci.*, vol. 47, no. 6, pp. 2451–2459, Dec. 2000, doi: 10.1109/23.903792.

[40] A. Jouni et al., "Proton-induced displacement damages in 2-D and stacked CMOS SPADs: Study of dark count rate degradation," *IEEE Trans. Nucl. Sci.*, vol. 70, no. 4, pp. 515–522, Apr. 2023, doi: 10.1109/TNS.2023.3248521.

[41] C. Inguimbert, A. Durand, T. Nuns, and K. Lemière, "Statistical spread on the displacement damage degradation of irradiated semiconductors," *Nucl. Instrum. Methods Phys. Res. Sect. B, Beam Interact. Mater. At.*, vol. 490, pp. 7–17, Mar. 2021, doi: 10.1016/j.nimb.2021.01.002.

[42] O. Gilard et al., "Damage factor for radiation-induced dark current in InGaAs photodiodes," *IEEE Trans. Nucl. Sci.*, vol. 65, no. 3, pp. 884–895, Mar. 2018, doi: 10.1109/TNS.2018.2799742.

[43] M. Benfante et al., "Electric field-enhanced generation current in proton irradiated InGaAs photodiodes," *IEEE Trans. Nucl. Sci.*, vol. 70, no. 4, pp. 523–531, Apr. 2023, doi: 10.1109/TNS.2023.3244416.

[44] M. Benfante, J.-L. Reverchon, C. Virmontois, S. Demiguel, and V. Goiffon, "Impact of irradiation temperature, doping, and proton energy on InGaAs photodiodes," *IEEE Trans. Nucl. Sci.*, vol. 71, no. 4, pp. 719–727, Apr. 2024, doi: 10.1109/TNS.2023.3340625.

[45] I. Jun et al., "Proton nonionizing energy loss (NIEL) for device applications," *IEEE Trans. Nucl. Sci.*, vol. 50, no. 6, pp. 1924–1928, Dec. 2003, doi: 10.1109/TNS.2003.820760.

[46] I. Jun, W. Kim, and R. Evans, "Electron nonionizing energy loss for device applications," *IEEE Trans. Nucl. Sci.*, vol. 56, no. 6, pp. 3229–3235, Dec. 2009, doi: 10.1109/TNS.2009.2033692.

[47] A. Y. Konobeyev, U. Fischer, Y. A. Korovin, and S. P. Simakov, "Evaluation of effective threshold displacement energies and other data required for the calculation of advanced atomic displacement cross-sections," *Nucl. Energy Technol.*, vol. 3, no. 3, pp. 169–175, Sep. 2017, doi: 10.1016/j.nucet.2017.08.007.

[48] C. Inguimbert, P. Arnolda, T. Nuns, and G. Rolland, "'Effective NIEL' in silicon: Calculation using molecular dynamics simulation results," *IEEE Trans. Nucl. Sci.*, vol. 57, no. 4, pp. 1915–1923, Aug. 2010, doi: 10.1109/TNS.2010.2049581.

[49] C. Inguimbert, P. Arnolda, T. Nuns, and G. Rolland, "'Effective NIEL' in silicon: Calculation using molecular dynamic simulation results," in *Proc. Eur. Conf. Radiat. Effects Compon. Syst.*, Brugge, Belgium, 2009, pp. 261–266, doi: 10.1109/RADECS.2009.5994592.

[50] C. Inguimbert, "Damage energy threshold anisotropy in non ionizing energy loss calculation," *IEEE Trans. Nucl. Sci.*, pp. 1–10, 2024, doi: 10.1109/TNS.2024.3376966.

[51] M. Benfante et al., "Proton radiation-induced dark current increase in InGaAs photodiodes," presented at the RADOPT, Toulouse, France, Nov. 2023.